

A window for water-hydrogen demixing on warm metal-rich sub-Neptunes

CAROLINE PIAULET-GHORAYEB ^{1,*} DANIEL P. THORNGREN ² ELIZA M.-R. KEMPTON ^{1,3} JUSTIN LIPPER,⁴
LESLIE ROGERS ¹ FERNANDA CORREA HORTA ¹ AND SHI LIN SUN⁴

¹*Department of Astronomy & Astrophysics, University of Chicago, 5640 South Ellis Avenue, Chicago, IL 60637, USA*

²*Department of Physics and Astronomy, Johns Hopkins University*

³*Department of Astronomy, University of Maryland, College Park, MD 20742, USA*

⁴*Institut Trottier de Recherche sur les Exoplanètes, Département de Physique, Université de Montréal, 1375 Avenue
Thérèse-Lavoie-Roux, Montreal, H2V 0B3, Canada*

ABSTRACT

Sub-Neptunes represent the largest exoplanet demographic, yet their bulk compositions remain poorly understood. Recent studies suggested that only very cold planets, such as Uranus and Neptune, could experience stratification of volatiles in their envelopes, implying that the envelopes of warmer sub-Neptunes instead have fully-miscible compositions. Here, we present ATHENAIA, an interior-atmosphere composition inference framework we leverage to assess the potential for water-hydrogen demixing on the $T_{\text{eq}} = 350$ K planet TOI-270 d, and more broadly for warm sub-Neptunes, using radiative-convective atmosphere models coupled to interior models. We find that the higher temperatures at which hydrogen and water demix in water-rich environments, combined with the shallower adiabatic gradients of water-rich envelopes, open a window for demixing on sub-Neptunes with bulk envelope metallicities of ~ 100 to $700\times$ solar, compatible with TOI-270 d. Demixing is easier to achieve on more massive and colder planets, but still broadly affects warm (330 to 500 K) metal-rich sub-Neptunes. Therefore, combining atmosphere metallicities with models of fully-miscible envelopes may lead to underestimated bulk envelope metallicities and mass fractions. Further, our modeling of TOI-270 d's envelope and interior reveals that, for a typical internal energy budget T_{int} of 25 K, the envelope-mantle boundary conditions likely preclude the presence of a molten magma ocean. This work encourages a reconsideration of the current paradigm for linking sub-Neptune atmospheres to their interiors and motivates further evolutionary modeling describing the onset of metallicity gradients in sub-Neptune envelopes.

Keywords: Exoplanets (498); Exoplanet atmospheric composition (2021); Exoplanet atmospheres (487); Exoplanet structure (495)

1. INTRODUCTION

One of the main goals of exoplanetary science consists in linking planetary compositions to formation conditions and evolutionary scenarios. This feat has proven particularly challenging for sub-Neptunes, despite their ubiquity as the most common type of exoplanets discovered by transit surveys (Howard et al. 2012; Batalha et al. 2013; Fulton & Petigura 2018). Sub-Neptune sizes range from approximately 2 to 4 Earth radii, with densities too low for pure-rock compositions, implying potentially thick gaseous envelopes. Yet, they are smaller than the solar system ice giants, limiting the prior as-

sumptions that can be made when interpreting their bulk makeup including, at the most basic level, whether their envelope is H/He-dominated, akin to gas giants, rich in ices deep below the observable atmosphere, similarly to Uranus and Neptune, or even metal-rich all the way to the upper atmosphere (Miller-Ricci et al. 2009; Rogers & Seager 2010).

An understanding of sub-Neptune interior compositions is critical to deciphering their origins at the population level, particularly when it comes to evaluating the relative importance of formation conditions (Kuchner 2003; Alibert & Benz 2017; Burn et al. 2024), and evolution through chemical interactions between the gas envelope and the mantle (Kite & Schaefer 2021; Schlichting & Young 2022) or atmospheric mass-loss driven by stellar irradiation (Rogers et al. 2021). Specifically, knowl-

Corresponding author: Caroline Piaulet-Ghorayeb
Email: carolinepiaulet@uchicago.edu

* E. Margaret Burbridge Postdoctoral Fellow

edge of sub-Neptunes’ envelope mass fractions and compositions will inform their overall metal/ice content, and is critical to interpreting their size and density distribution (Luque & Pallé 2022; Neil et al. 2022; Rogers et al. 2023) as well as modeling envelope mass-loss (Gupta & Schlichting 2020; Owen & Wu 2017). Further, envelope extent and metal content both impact the planet’s thermal structure, dictating the molten or solid state of the mantle which drastically impacts the efficiency of dissolution/outgassing of volatile species (Lichtenberg et al. 2021; Werlen et al. 2025b), and sets the planet’s cooling rate over its thermal evolution.

Given the vast array of processes shaping sub-Neptune atmospheres and our little grasp on their relative importance from a theoretical standpoint, observational constraints on sub-Neptune envelope properties are crucial. A growing sample of sub-Neptunes now have both mass and radius measurements precise enough to infer envelope mass fractions via interior-atmosphere structure modeling, traditionally assuming either H/He-dominated envelopes, pure-water hydrospheres, or layered structures with water at high pressures underlying the gas-phase hydrogen (e.g. Lopez & Fortney 2014; Zeng et al. 2019; Turbet et al. 2020; Aguichine et al. 2021; Madhusudhan et al. 2020). The resulting envelope mass fraction estimates are however extremely degenerate with the envelope metallicity, with uncertainties of about an order of magnitude on the mass budget of the envelope between the two extremes of H/He-dominated solar-metallicity gas, and e.g. pure-water envelope scenarios. Atmosphere studies, which traditionally probe the upper layers of planetary envelopes in transmission at \sim mbar pressures, have been proposed as a way to resolve this degeneracy. However, the traditional view of layered structures, with most volatiles confined to the high pressure region of the envelope and inaccessible to observations, has limited the information content that transmission spectroscopy could provide as to the metal or water content of the entire envelope.

Recent theoretical work has shown that what was traditionally thought of as the “hydrogen-water boundary” in sub-Neptune envelopes, i.e. the pressure and temperature at which the hydrogen-rich upper envelope transitions to a water-rich lower layer, occurs at conditions where water would be in the supercritical phase because of the warming greenhouse effect of the hydrogen-rich gas (Madhusudhan et al. 2020; Piaulet et al. 2023). Only for the coldest planets can water condense out into clouds in the atmosphere, or in even more extreme cases where the hydrogen layer is extremely thin, form a liquid ocean (referred to as “hycean” worlds; Madhusudhan et al. 2021; Innes et al. 2023). Since experiments and

density-functional-theory (DFT) simulations supported the miscibility of supercritical water with hydrogen (Seward & Franck 1981; Bergermann et al. 2024; Gupta et al. 2024), a picture has emerged where most warm sub-Neptunes would have fully miscible envelopes with hydrogen and water well-mixed from the supercritical phase all the way to the gas probed at lower pressures in transmission spectroscopy (Nixon et al. 2024; Innes et al. 2023; Pierrehumbert 2022; Benneke et al. 2024). This perspective opened up the exciting possibility that the atmospheric conditions measured on sub-Neptunes may reflect the bulk envelope composition, and further facilitate breaking the core mass/envelope mass degeneracy.

However, both experimental data and theoretical predictions relying on numerical calculations support the existence of a “solvus”, also known as the “critical curve”, in temperature-pressure space, beyond which water and hydrogen, even at high pressures, are no longer miscible and would form two distinct phases (Seward & Franck 1981; Bergermann et al. 2024; Gupta et al. 2024). Since the stability of coexisting hydrogen and water also depends on the mixture composition, this can give rise to “demixing”, a process whereby two fluids cannot thermodynamically mix into a homogeneous phase. Demixing is distinct from a phase transition (such as water condensation), or what is traditionally thought of as stratification via rainout (driven by gravitational separation).

Demixing has already been shown to impact the interior structures and thermal evolution of Uranus and Neptune in the solar system, leading to envelope compositional gradients due to H/He and H/H₂O phase separation (Nettelmann et al. 2011; Amoros et al. 2024; Arevalo 2025). Demixing could similarly affect the atmospheres of sub-Neptunes and lead to compositional gradients that would break the link between bulk envelope and upper atmosphere metallicity, and impact both the susceptibility of sub-Neptune atmospheres to mass-loss and their cooling rates. Recent theoretical predictions extended the range of thermodynamical conditions over which this critical curve is constrained to those relevant for sub-Neptune interiors (Gupta et al. 2024), opening the possibility to assess their propensity to demixing at the population level.

In particular, the small ($2.2 R_{\oplus}$, Eylon et al. 2021) sub-Neptune TOI-270 d, with its low insolation resulting in a zero-albedo equilibrium temperature of about 380 K, has received considerable scrutiny since the detection of volatiles such as methane, carbon dioxide, as well as potentially large amounts of water in its hydrogen-dominated, but metal-enriched atmosphere (Benneke

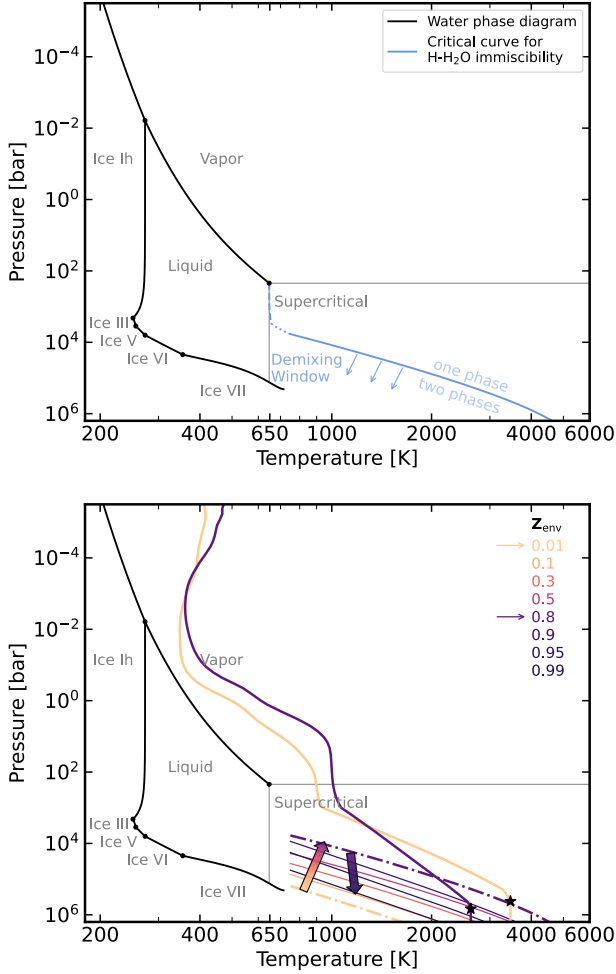


Figure 1. Illustration of the demixing window concept. *Top panel:* Water phase diagram (black lines) with labeled regions; the critical curve (blue) indicates the highest temperature for single-phase H-H₂O mixing, compiled from low-pressure data (dashed, Seward & Franck 1981) and high-pressure data (solid, Gupta et al. 2024), with interpolation (dotted). Envelope T-P profiles below the blue line can experience demixing for some compositions. *Bottom panel:* Demixing window at different metallicities. High-pressure H-H₂O coexistence curves (colored), for various envelope metallicities Z_{env} , show that the window for immiscible conditions is maximal for metallicities near $Z \sim 0.8$, but recedes for lower and higher metallicities (illustrated by colored arrows). Example T-P profiles for a $5.14 M_{\oplus}$ planet (TOI-270 d-like irradiation, $A_b = 0$), with 16% envelope mass and metallicity of either 0.01 ($1\times$ solar; orange) or 0.8 ($\sim 300\times$ solar; purple), are shown, with dash-dotted linestyles for the corresponding coexistence curves. At low metallicity, the profile does not intersect the coexistence curve (up to the mantle-envelope boundary, star marker), but for $Z_{\text{env}} = 0.8$, it does, implying that for stable conditions, the atmosphere metallicity is likely lower than that of the bulk envelope.

et al. 2024; Holmberg & Madhusudhan 2024; Felix et al. 2025; Nixon et al. 2025; Constantinou et al. 2025). In terms of its interior structure, the scenarios proposed for TOI-270 d range from Hycean conditions (Holmberg & Madhusudhan 2024), to a fully-miscible envelope (Benneke et al. 2024). The photospheric temperature measured on TOI-270 d now disfavors the formation of a liquid water ocean except perhaps on the nightside (“dark Hycean world” scenario, Madhusudhan et al. 2021; Constantinou et al. 2025; Rigby & Madhusudhan 2025).

Although initial estimates claimed that demixing should not occur even on the colder ~ 255 K sub-Neptune K2-18 b (Gupta et al. 2024), independent modeling exploration suggested that both K2-18 b and TOI-270 d could experience demixing (Howard et al. 2025). However, the latter work described the behavior of water in the interior of the planet using an equation of state (More et al. 1988) that has been superseded by more recent prescriptions (Mazevet et al. 2019). The differences in the predicted temperatures in sub-Neptune interiors, using the updated adiabatic gradients, range from hundreds to more than 1000 K (Aguichine et al. 2021; Howard et al. 2025). Further, although the impact of using real atmosphere models, compared to predictions from profiles combining adiabats with parameterized profiles for the upper radiative regions, was shown to have important impacts on predicting sub-Neptune radii and their thermal evolution, especially for metal-rich compositions (Aguichine et al. 2024). Yet, no modeling effort has yet used fully self-consistent radiative-convective atmosphere models coupled with interior models to assess the susceptibility of sub-Neptune envelopes to demixing across the mass-radius diagram.

The contrasting predictions ranging from fully-miscible envelopes for warm sub-Neptunes, to demixing-driven compositional gradients for the more massive and much less irradiated (less than 0.3% of Earth’s irradiation) solar system ice giants, suggests the existence of a “demixing window” (Fig. 1): planetary conditions where envelope metallicity gradients could exist. The evaluation of this compositional transition is essential to assess the extent to which, in particular, water abundances and metallicity estimates from transmission spectroscopy can be translated to bulk envelope water contents. In this study, we apply full-planet models combining interior models with state-of-the-art water EOS, and self-consistent atmosphere models in radiative-convective equilibrium to evaluate the temperature/pressure conditions in sub-Neptune atmospheres and their composition-, internal heating-, and irradiation-dependent susceptibility to demixing. The aims of this study are two-fold: (1) provide a frame-

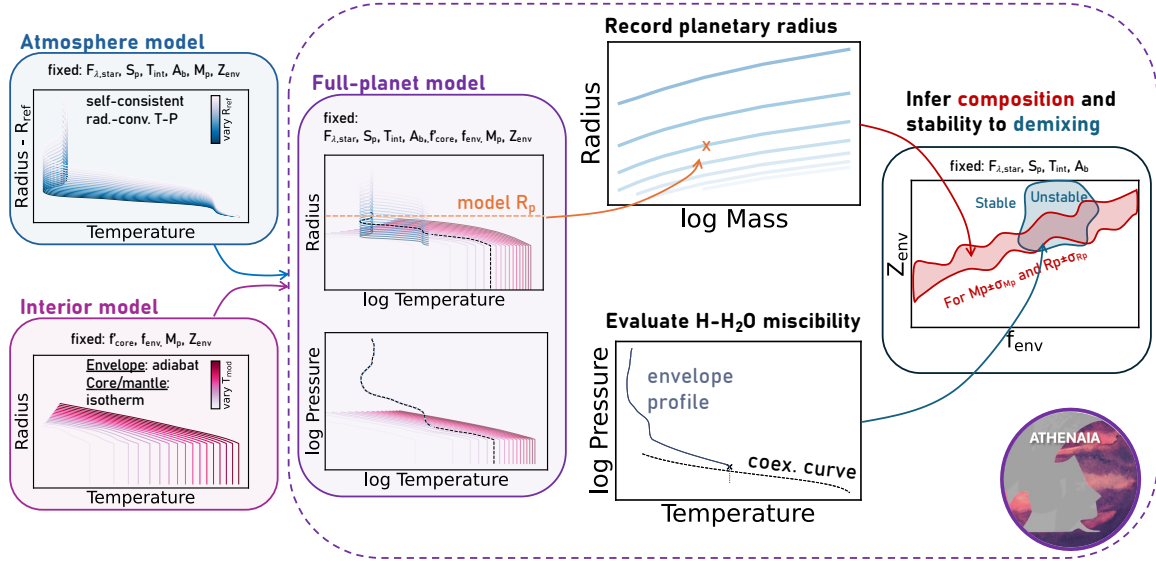


Figure 2. Illustration of the workflow for the construction of coupled interior-atmosphere models with ATHENAIA. For each composition, atmosphere models are calculated with SCARLET (top left) and interior models following the model from Thorngren & Fortney (2019). Then we couple them with ATHENAIA by finding the R_{ref} (atmosphere model) and T_{mod} (interior model) that minimize δ_{TPR} (see Eq. 5). The radius at 20 mbar is extracted to construct constant-composition mass-radius curves, while the pressure-temperature profile of the envelope is used to evaluate the stability to demixing by comparing to the corresponding H-H₂O coexistence curve (dashed). Finally (right panel), given planetary mass and radius, the range of potential compositions is mapped to $f_{\text{env}} - Z_{\text{env}}$ space (red) and compared to the map of conditions where envelopes are (un)stable against demixing (blue).

work for the systematic evaluation of whether demixing occurs on a given sub-Neptune planet provided mass, radius, energy budget, and potential atmospheric constraints, and (2) delineate the demixing conditions in mass, radius, and composition space in order to support population-level interpretation of sub-Neptune compositions and evolutionary models.

This paper is organized as follows. In Section 2, we describe our methods for the atmosphere and interior modeling and the evaluation of hydrogen-water miscibility. In Section 3, we describe our grid of full-planet models and the composition inference algorithm. We discuss our results in terms of the envelope conditions on TOI-270 d in Section 4, and implications for the sub-Neptune population in Section 5. We compare our results to previous work in Section 6, discuss potential caveats in Section 7 and summarize our findings in Section 8.

2. FULL-PLANET MODELING

This study aims to determine whether well-mixed envelope compositions are stable on planets with varying bulk properties, compositions, and energy budgets, or whether compositional gradients should be expected throughout the envelope. We construct full-planet models with envelopes that are well-mixed from the mantle-envelope (MEB) boundary up to the top of the atmo-

sphere, before evaluating whether the conditions for H-H₂O coexistence in a single phase are met. In contrast with previous work, we evaluate hydrogen-water miscibility using interior models coupled with atmosphere models in radiative-convective equilibrium with a composition identical to that of the deep envelope. While previous work assumed either stratified water- and H₂-dominated layers (e.g. Madhusudhan et al. 2020), or well-mixed envelopes and atmospheres with uniform compositions throughout (e.g. (Nixon et al. 2024)), we perform a systematic evaluation of the phase stability of the mix to evaluate the validity of either assumption across expected sub-Neptune conditions.

We present ATHENAIA, the ATmosphere-iNterior bAYesian Inference frAMework (Fig. 2). The ATHENAIA framework builds up on an earlier version of the code that was tailored to planets with a layered structure where hydrogen and water are stratified (Piaulet et al. 2023; Roy et al. 2022; Benneke et al. 2024). ATHENAIA performs three main tasks: (1) self-consistent modeling of full-planet profiles, given atmosphere and interior modeling frameworks and input parameters for the bulk planetary composition, properties, and energy budget; (2) Bayesian inference of bulk planetary compositions, given known stellar and planetary properties; and (3) evaluation of water-hydrogen miscibility throughout the planetary envelope. Using

ATHENAIA, we introduce the concept of a “demixing window”, the region of parameter space where planetary conditions are no longer consistent with fully miscible envelopes. Each of these components are presented in the following sub-sections.

Parameter	Value
Star: TOI-270	
Spectral Type	M3.0V
Effective temperature T_{eff} [K]	3506 ± 70
Metallicity [Fe/H]	-0.2 ± 0.12
$\log g$ [cm/s^2]	4.872 ± 0.026
Planet: TOI-270 d	
Radius R_p [R_{\oplus}]	$2.216^{+0.065}_{-0.064}$
Mass M_p [M_{\oplus}]	4.78 ± 0.43
Semi-major axis a_p [AU]	0.0742 ± 0.0014
Insolation S_p [S_{\oplus}]	3.5 ± 0.4
Irradiation Temperature T_{irr} [K]	381 ± 10
T_{eq} ($A_B=0.2$) [K]	361 ± 10
T_{eq} ($A_B=0.4$) [K]	336 ± 9

Table 1. Stellar and planetary parameters for the TOI-270 system used in this work. The stellar parameters and planet mass are from [Eylon et al. \(2021\)](#), while the planetary radius and orbital parameters are from the fit to the JWST/NIRISS SOSS data ([Benneke et al. 2024](#)). We report the derived irradiation temperature (zero-Bond albedo equilibrium temperature) and representative equilibrium temperatures for the two other albedo values used in this work. We use the median parameters to describe the stellar irradiation, but marginalize over the distribution of possible masses and radii accounting for their uncertainties to infer the range of compositions compatible with TOI-270 d’s parameters.

2.1. Interior modeling

For the interior portion of our full-planet models, we use one-dimensional interior structure models ([Thorngren et al. 2016](#); [Thorngren & Fortney 2019](#)) in order to derive profiles of temperature, pressure, radius, and density given bulk planetary properties. These models consist of an inert rock/iron interior with an Earth-like fraction $f'_{\text{core}} = 1/3$ of the mass contained in an iron core and $2/3$ in a silicate mantle, overlaid with a homogeneous convective envelope that has a metallicity Z_{env} regulated by the amount of H_2O mixed with the H, He, and makes up a fraction f_{env} of the total planet mass. The models solve the equations of hydrostatic equilibrium, mass conservation, and the equation

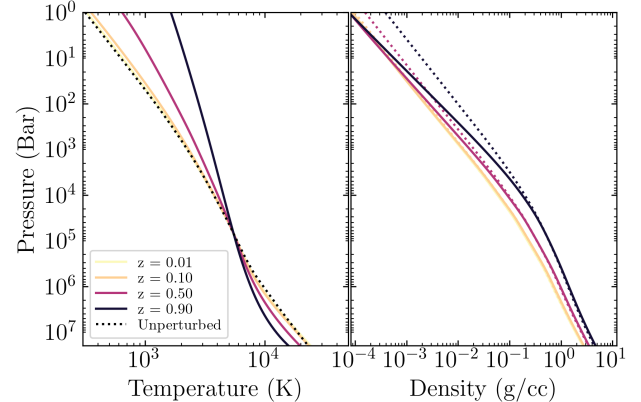


Figure 3. The adiabatic pressure-temperature profiles used for the water/H/He mixtures in our interior models at various compositions, which were computed through integration of the computed adiabatic gradient. These are compared against the approximation that the P-T profile is the same as for $Z=0$ (pure H/He, dotted line). The densities only differ significantly at low pressures, but the temperature gradient is significantly different by $Z=0.5$, which affects the thermal evolution.

of state (EOS). For the latter we use [Chabrier et al. \(2019\)](#) for the H/He mix, [Mazevet et al. \(2019\)](#) for H_2O , and [Thompson \(1990\)](#) for rock and iron.

The interior temperature-pressure profile is calculated assuming convection throughout the deep H/He/ H_2O envelope, and is assumed to be isothermal below the MEB (with little impact on the radius estimates central to this work). The water and H/He equations of state were mixed using the additive-volumes rule, with the adiabatic profile obtained from numerical integration (analogous to [Nettelmann et al. 2008](#)) of the adiabatic gradient, which was in turn computed from the density and internal energy values provided by the original EOS (see [Thorngren 2019](#), Sec. 1.4.1 for more details) as a function of pressure and temperature. This approach is an upgrade from e.g. [Thorngren & Fortney \(2019\)](#), which used H/He adiabats without perturbation by the mixed metals; a comparison is shown in Fig. 3.

These standalone interior models do not include atmosphere models to serve as an upper boundary condition in temperature-pressure space, so they are calculated for various reference temperatures T_{mod} , here taken at 10 bar, which set the conditions for the adiabatic profile in the envelope. This means that the thermal evolution of the adiabat is indexed by the 10-bar potential temperature, rather than the specific entropy s as in e.g. [Thorngren et al. \(2016\)](#), but these approaches are equivalent. The interior models are calculated over a grid of Z_{env} , planet masses M_p , envelope mass fractions f_{env} , and T_{mod} . Only the subset of T_{mod} values where the

temperature at the link point between the atmosphere model and deep envelope (interior model) is compatible with predictions given the planet’s irradiation level and internal temperature T_{int} (see next subsection) are actually represented in the final models we produce for this work.

2.2. Atmosphere modeling

In parallel with the grid of interior models, we calculate a grid of atmosphere models that will describe the behavior of the temperature/pressure/radius profiles at lower pressures ($\lesssim 1$ kbar), accounting for both convective and radiative energy transport. We use a version of the SCARLET atmosphere forward modeling and retrieval framework (Benneke & Seager 2012; Benneke 2013; Benneke et al. 2019) adapted for the computation of self-consistent models up to the high metallicities required to describe sub-Neptunes, and amenable for coupling with interior models (Piaulet et al. 2023; Piaulet-Ghorayeb et al. 2024).

The calculation of a self-consistent radiative-convective atmosphere model takes as inputs a stellar spectrum, atmospheric composition, and planetary properties such as mass M_p , radius R_{ref} at a set reference pressure p_{ref} , bolometric insolation S_p , internal temperature T_{int} , and Bond albedo A_B .

SCARLET solves iteratively the hydrostatic equilibrium and radiative transfer equations until the energy deposited in the planet’s atmosphere at the lower boundary (regulated by T_{int}) and from the star’s irradiation (dependent on the stellar spectrum, atmospheric composition, S_p , and A_B) balance in each layer. We use a version of SCARLET that lifts the assumption of constant mass throughout the atmosphere (Piaulet et al. 2023) and rather accounts for the mass contained in each atmosphere layer when solving hydrostatic equilibrium. We also implement new methods for the convergence of the radiative-convective profiles and adiabatic gradient prescriptions, appropriate for the high levels of metal enrichment covered in our modeling exploration (see Section A). In order to couple these atmosphere models with the appropriate interior models given any f'_{core} , f_{env} , we calculate for each $Z_{\text{atm}} = Z_{\text{env}}$, M_p , T_{int} , and A_B atmosphere models with R_{ref} (set at $p_{\text{ref}} = 1$ kbar) varied over the range of values covered by the interior model grid. The hydrostatic equilibrium and radiative transfer equations are solved independently for each R_{ref} .

2.2.1. Atmospheric composition

The SCARLET models assume well-mixed compositions, with the volume mixing ratios (VMRs) of the three component gases H_2 , He , and H_2O kept constant

throughout the atmosphere. H_2O is used as the metallicity proxy, and we translate a chosen $Z_{\text{atm}} = Z_{\text{env}}$ to VMRs assuming the protosolar Y/X ratio of $r = \text{Y}/\text{X} = 0.275/0.725$ is maintained (Lodders 2010). Letting

$$X = \frac{1 - Z_{\text{env}}}{1 + r} \quad (1)$$

and

$$Y = rX = \frac{r(1 - Z_{\text{env}})}{1 + r}, \quad (2)$$

we obtain:

$$\text{VMR}_S = \frac{X_S/m_S}{D} \quad (3)$$

where S is either H_2 , He , or H_2O , substituting for X_S : X , Y , or Z_{env} , respectively, and

$$D = X/m_{\text{H}_2} + Y/m_{\text{He}} + Z_{\text{env}}/m_{\text{H}_2\text{O}}. \quad (4)$$

2.3. Link between atmosphere and interior models

In order to obtain full-planet models for a given planetary energy budget, mass, envelope composition Z_{env} , and relative mass budgets of iron, silicates, and $\text{H}/\text{He}/\text{H}_2\text{O}$ envelope (set by f'_{core} and f_{env}), we employ an algorithm to optimize the choice of interior and atmosphere models among the set calculated for those parameters. This method consists in finding T_{mod}^* and R_{ref}^* that minimize the δ_{TPR} distance, defined as:

$$\delta_{\text{TPR}} = \sqrt{|\delta T|_{P_{\text{link}}}^2 + |\delta T|_{R_{\text{link}}}^2} \quad (5)$$

with P_{link} , R_{link} the atmosphere model’s pressure in bars and radius in Earth radii at the pressure level where the link with the interior model happens. This pressure is either that of the radiative-convective boundary, P_{rcb} (if $P_{\text{rcb}} < 1$ kbar), or 1 kbar otherwise. $|\delta T|_{P_{\text{link}}}$ is the temperature difference between each of the atmosphere models (for each R_{ref}), and each of the interior models (for each T_{mod}). $|\delta T|_{R_{\text{link}}}$ is defined similarly by comparing the temperatures of the atmosphere and interior models at the radius where $P = P_{\text{link}}$ in the atmosphere model. The full planetary profiles for temperature/pressure/radius/density are then set to be the atmosphere profiles of the best-match atmosphere model R_{ref}^* at pressures lower than P_{link} , and the interior profiles of the best interior model T_{mod}^* at deeper pressures. The planetary radii at 1, 10, and 20 mbar are recorded for each full-planet composition scenario. When displaying the resulting constant-composition curves in mass-radius space, or comparing to TOI-270 d’s radius, we use the 20 mbar radii for easy comparison with previous works (Lopez & Fortney 2014; Benneke et al. 2024).

In the rare cases that correspond to very low f_{env} where the core-envelope boundary (CEB) between the

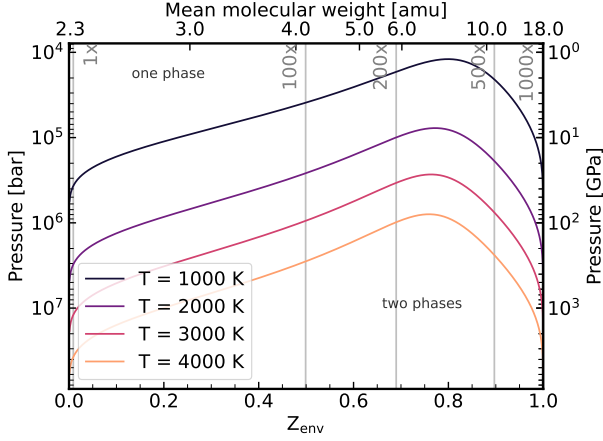


Figure 4. Coexistence curves for hydrogen and water in pressure-metallicity space, for 4 different temperatures. Vertical lines indicate 1 to 1000 \times solar metallicity. The corresponding mean molecular weight values are indicated at the top. Demixing is easier to achieve in colder envelopes with moderate metal enrichments.

core/mantle and the envelope happens at pressures that are shallower than the RCB, or shallower than 1 kbar if the RCB is not shallower than 1 kbar, we instead link the interior and atmosphere models that minimize δR_{CEB} , the difference in radius at the CEB pressure (identified in the interior model).

2.4. Evaluation of hydrogen-water miscibility

Water-hydrogen demixing in a planetary envelope occurs when local thermodynamic conditions do not allow for the coexistence of hydrogen and water in a single miscible phase. This typically leads to metallicity gradients, with more metal-rich material in the deeper atmosphere, such that a steady state is reached where the atmosphere composition at each pressure is stable against further demixing. The stability of planetary envelopes to demixing results from a complex interplay between energy budget and composition. Generally, hotter planets will be stable against demixing over vast regions of the parameter space, since the instability occurs when the temperature at a given pressure is *lower* than the water-hydrogen coexistence curve. The coexistence curves themselves are highly compositionally-dependent, with variations in the demixing conditions spanning thousands of K in the deep planetary interior, depending on the exact metallicity value (Figs. 1 and 5). Meanwhile, although the upper atmospheres of more metal-rich planets will generally be warmer, the adiabatic temperature gradient governing the temperature as a function of depth in the convective envelope becomes *shallower* at higher metallicities (Fig. 5), resulting in an overall higher propensity of envelopes with

high metal content to demixing (all else being equal). Combined with the coexistence curves being pushed to much higher temperatures around $Z_{\text{env}} \in [0.6, 0.8]$ (approximately 140 to 300 \times solar metallicity)⁵, these factors can open the demixing window presented in this work.

For each combination of model parameters, ATHENAIA assesses the stability of a fully-mixed envelope against hydrogen-water demixing. Within the scope of this study, we aim to evaluate the range of well-mixed envelope compositions where hydrogen and water are miscible all the way to the top of the rocky mantle (MEB pressure). We interpret profiles where the miscibility criterion is not met throughout the entire envelope as compositional gradients from a metal-poor upper envelope to the more metal-rich deep envelope. For the demixing criterion, we use the recent DFT calculations from Gupta et al. (2024) that extend up to the high pressures and temperatures expected in sub-Neptune interiors.

The criterion for fully miscible envelopes is that, throughout the entire range of pressures up to the MEB, the temperature profile of the planet lies above the composition-dependent hydrogen-water coexistence curve (Figs. 1 and 2). For the computation of the coexistence curves, we calculate the compositional parameter x_{H_2} describing the H_2 - H_2O conditions from the value of Z_{env} :

$$x_{\text{H}_2} = \frac{N_{\text{H}_2}}{N_{\text{H}_2} + x_{\text{H}_2\text{O}}} \quad (6)$$

In practice, we adopt the following relationships:

$$x_{\text{H}_2} = 1 - \frac{2\beta}{1 + 2\alpha - 4\alpha\beta}; \quad (7)$$

with:

$$\alpha = \frac{He}{H_{\text{free}}} = \frac{Y}{1 - Y} \frac{m_H}{m_{He}} \quad (8)$$

and:

$$\beta = \frac{O}{H_{\text{bound+free}}} = \frac{\alpha m_{He} + m_H}{m_{\text{H}_2\text{O}} (1/Z_{\text{env}} - 1) + 2(\alpha m_{He} + m_H)}. \quad (9)$$

Here, α describes the ratio (by number) of He over “free” H (i.e., not bound in H_2O). Y is defined following Eq. 2.2.1, and m_X is the mass of species X . Given $x_{\text{H}_2}(Z_{\text{env}})$, we calculate the temperature-dependent quantities W_v (describing the pressure-dependent term in the Gibbs free energy calculation) and λ (describing the asymmetry in the coexistence curves) following Eq.

⁵ Throughout this study, metallicities relative to solar are computed from the envelope O/H ratio.

(6-7) in Gupta et al. (2024), to finally compute the variable y :

$$y = \frac{x_{\text{H}_2}}{x_{\text{H}_2} + \lambda(1 - x_{\text{H}_2})} \quad (10)$$

which is then translated into the pressure level of the coexistence curve at each queried temperature over the range of validity (750 to 6000 K) following Eq. (8) in Gupta et al. (2024) using the 50th percentile fitted values in their Table 1. For the final evaluation, we assess whether over the range of pressures spanned by both the envelope (above the MEB) and the coexistence curve, there exists any point where the temperature in the envelope drops below the coexistence curve, which defines a profile as unstable against demixing. In practice, we record for each profile across the full parameter grid explored the minimum distance D_{\min} (in units of K) between the envelope temperature profile and the coexistence curve and draw the contours of the “demixing window” in $f_{\text{env}}\text{-}Z_{\text{env}}$ space for each combination of planet mass and Bond albedo as interpolated contours of $D_{\min} = 0$ (Figs. 6 and 7).

3. PLANET COMPOSITION INFERENCE

Our planetary composition inference framework relies on the computation of a grid of coupled interior-atmosphere models that predict planetary temperature, density, and radius as a function of pressure. Within the context of this work, the grid setup is tailored to the exploration of the potential for envelope compositional gradients even on warm sub-Neptunes, as described below. Beyond this broad parameter space exploration, we evaluate the specific bulk parameters consistent with TOI-270 d’s known properties and whether these could lead to potential demixing, in order to assess claims of a fully miscible envelope.

3.1. Grid setup

Our model grid focuses on planets with irradiation levels comparable to TOI-270 d, warm enough to avoid both water condensation at the surface and in the atmosphere under conditions compatible with the JWST-inferred compositional constraints except in high-albedo scenarios (Holmberg & Madhusudhan 2024; Benneke et al. 2024; Felix et al. 2025; Constantinou et al. 2025), further supported by our modeling (Fig. 6).

For the core and mantle, we fix the composition to an Earth-like mass fraction $f'_{\text{core}} = 0.325$ (following the terminology in Piaulet-Ghorayeb et al. 2024) of the core and mantle underlying any of the envelopes modeled for this work. In terms of the energy budget, we fix the orbital distance and incident stellar spectrum to those of TOI-270 d (Table 1, with the closest stellar model

in the PHOENIX grid; Husser et al. 2013) and adopt $T_{\text{int}} = 25$ K as the lower boundary condition for atmosphere models (discussed in Section 7). We vary the planetary Bond albedo between 0 and 0.4, with the upper limit of 0.4 informed by the range of photosphere temperatures of $\sim 330 - 350$ K retrieved by transmission studies (Benneke et al. 2024; Felix et al. 2025; Constantinou et al. 2025). Envelope compositions are varied from solar-metallicity H/He-dominated all the way to pure-water envelopes. Finally, the range of envelope mass fractions and planetary masses considered span the full range of expected surface gravities across the sub-Neptune regime (see Table 2). For each model, we follow the steps outlined in Section 2 (Fig. 2) to record the full-planet profiles (Fig. 5) and planetary radii to construct mass-radius relationships.

A_B	M_p [M_{\oplus}]	Z_{env}	$\text{H}_2\text{O VMR}$	f_{env} [%]
0.0	2.87	0.01	0.0013	0.0010
0.2	4.23	0.10	0.0142	0.0018
0.4	5.14	0.35	0.0652	0.0034
	6.24	0.40	0.0795	0.0061
	9.20	0.50	0.1147	0.0113
	13.56	0.55	0.1367	0.0206
	20.00	0.60	0.1627	0.0378
		0.65	0.1940	0.0693
		0.70	0.2322	0.1269
		0.75	0.2799	0.2325
		0.80	0.3414	0.4259
		0.85	0.4234	0.7802
		0.90	0.5384	1.4293
		1.00	1.0000	2.6186
				4.7973
				8.7887
				16.101
				29.497
				54.039
				99.000

Table 2. Planetary parameters spanned by the model grid. The $\text{H}_2\text{O VMR}$ values are derived from each model’s Z_{env} . The envelope mass fractions span 10^{-5} to 1 in log space. For all models, we use $T_{\text{int}} = 25$ K and $f'_{\text{core}} = 0.325$.

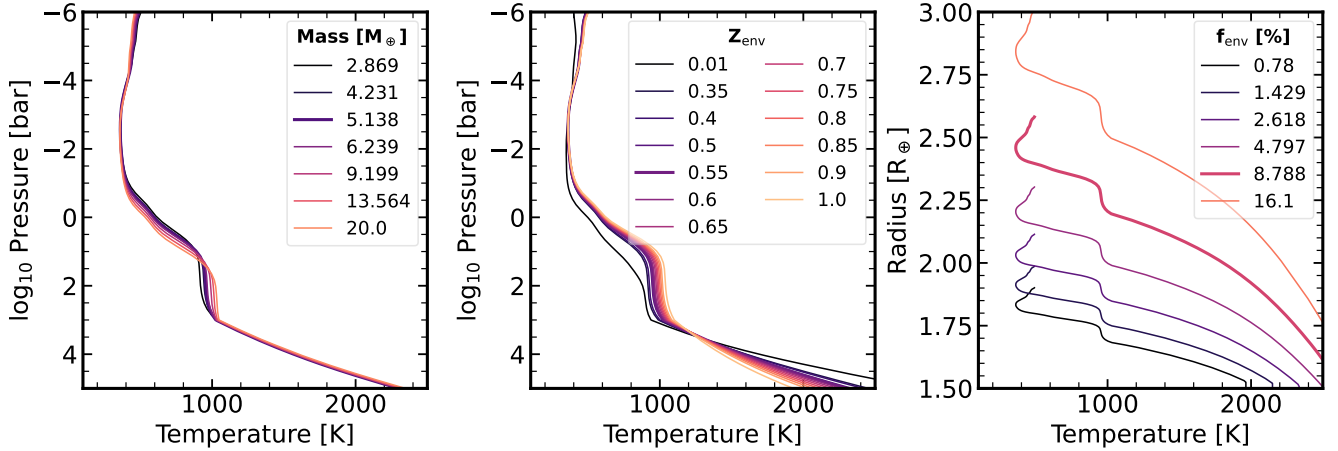


Figure 5. Impact of physical parameters varied across the grid on the pressure-temperature and pressure-radius profiles. The left, middle, and right panel illustrate the impact of varying the planet mass, envelope metallicity, and envelope mass fraction respectively. Aside from the parameter varied in each panel, all other parameters are kept fixed to $A_B = 0$, $M_p = 5.14 M_\oplus$, and $f_{\text{env}} = 8.79\%$. Increasing the planetary albedo shifts the atmosphere profile to lower temperatures, as illustrated in Fig. B1.

3.2. Metallicity-Envelope Mass Fraction Inference

We use ATHENAIA to perform inference of the range of envelope mass fractions and metal contents consistent with TOI-270 d’s observed mass, radius, and irradiation to evaluate its compatibility with a fully-miscible envelope. ATHENAIA inherits its Bayesian inference framework for envelope and bulk properties from previous work (Piaulet et al. 2023, see applications in Roy et al. 2022; Benneke et al. 2024). The method is briefly summarized below.

One grid of planetary radii is generated for each value of A_B that we explore, spanning the dimensions ($M_p; \log_{10} f_{\text{env}}; Z_{\text{env}}$). From each grid, an interpolator is created to infer planetary radii in-between grid points via linear interpolation. We first construct a likelihood grid by finely sampling all three dimensions, and calculating for each the Gaussian likelihood value knowing the planetary radius and its uncertainty (Table 1). Then, we compute the prior which is uniform with $\log_{10} f_{\text{env}}$ and Z_{env} , but Gaussian with M_p in order to marginalize over the mass uncertainty (Table 1). Finally, we extract the coordinates in the 2D $f_{\text{env}}-Z_{\text{env}}$ space corresponding to the 68.2% and 95.4% confidence intervals from the Bayesian posterior distribution (Fig. 6).

4. APPLICATION TO TOI-270 D

We demonstrate on TOI-270 d our approach for evaluating the potential for demixing in warm sub-Neptune interiors using ATHENAIA. We combine information from mass, radius, and atmosphere characterization with constraints on the range of interior structures where fully miscible envelopes would be unstable.

4.1. Inferred envelope properties

We obtain statistical constraints on the range of envelope mass fractions and envelope metallicities that are compatible with TOI-270 d’s bulk properties and irradiation (Fig. 6). The posterior distribution in this 2D space exhibits the well-known sub-Neptune compositional degeneracy: the planet can be explained either by a 1–3 percent-by-mass (wt%) H/He-rich solar-metallicity atmosphere, or at the other extreme by a 30–60 wt% pure-water atmosphere. Assuming that the atmosphere metal mass fraction Z_{atm} measured with JWST is representative of the envelope metallicity, we reproduce the previously-reported $\sim 10\%$ envelope mass fraction (Benneke et al. 2024).

4.2. Potential for compositional gradients

We map in the same 2D $f_{\text{env}}-Z_{\text{env}}$ space the demixing window inferred for the two masses in our grid closest to TOI-270 d: 4.23 and 5.14 M_\oplus (compared to TOI-270 d’s $M_p = 4.78 \pm 0.43 M_\oplus$). We find that in these conditions, demixing can happen on TOI-270 d for $Z_{\text{env}} \in [0.5 - 0.95]$ (100 to 700 \times solar metallicity), with the exact bounds depending on the assumption on A_B .

Given the considerable overlap in this demixing space with the inferred upper atmosphere metallicity (Fig. 6), our modeling suggests that TOI-270 d’s envelope may very well exhibit compositional stratification. In this case, TOI-270 d’s bulk envelope metallicity would be higher than the estimate from the upper envelope due to demixing. Our zeroth-order attempt at mapping the extent of the compositional gradient required to observe any given photospheric Z_{atm} suggests a true envelope bulk metallicity of up to $Z_{\text{env}} \sim 0.9$ (see Appendix

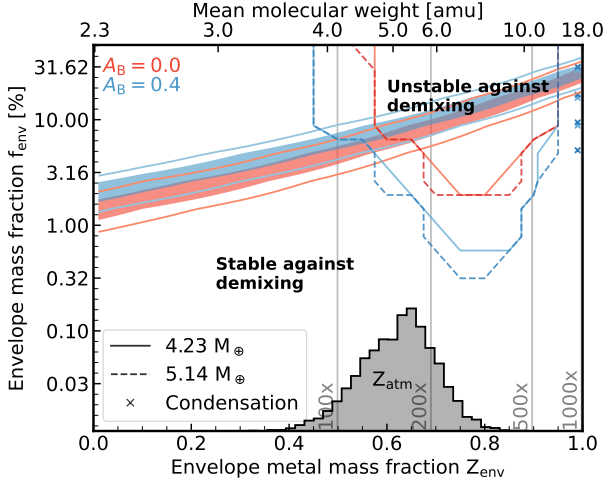


Figure 6. Joint constraints on the envelope mass fraction and envelope metal content of TOI-270 d. The red (blue) contours spanning the full range of potential envelope metallicities represent the 1 and 2σ composition constraints for a Bond albedo of 0 (0.4), based on the mass, radius, and insolation of TOI-270 d obtained with ATHENAIA. The contours in the top right corner outline the region of the parameter space where fully-mixed compositions are unstable (red for $A_B = 0$, blue for $A_B = 0.4$, line style encodes planet masses bracketing TOI-270 d). The gray histogram is the posterior distribution on the atmosphere metallicity of TOI-270 d from JWST transmission spectroscopy (Benneke et al. 2024). Over the range of atmosphere metal mass fractions allowed by the transmission spectrum, the $Z_{\text{env}}-f_{\text{env}}$ posterior distribution overlaps with the demixing window, where envelope compositional gradients can occur. Vertical grey lines show the locations of various metallicity enrichments relative to solar (labeled). Crosses (slightly offset to the left for clarity) indicate the models where the water condensation curve is crossed: they lie beyond the demixing window and do not affect the conclusions.

Section, Figure B2, which would require a less massive planetary core than previously inferred, with an envelope up to twice as massive. Alternatively, if the true $Z_{\text{atm}} < 0.55$, or if the thermal evolutionary state of TOI-270 d maintains its interior hotter than the $T_{\text{int}} = 25$ K inferred here, the fully-miscible envelope scenario may still hold.

4.3. Plausibility of mantle melting

We additionally apply our ATHENAIA models to an evaluation of the physical conditions at the MEB. The molten or solid state of the planetary mantle is of paramount importance because of its impact on the atmospheric composition. In the presence of a molten mantle (Kite & Schaefer 2021; Schlichting & Young 2021), the relative solubilities of the volatiles present (Lichtenberg 2021) and the mantle composition dictate how volatiles will be distributed between the mantle and

the overlying gas. Water, in particular, has a solubility orders of magnitude larger than most carbon-bearing species, impacting the atmospheric C/O ratios expected on sub-Neptunes with vs. without magma oceans at the envelope-atmosphere boundary (Werlen et al. 2025a,b).

Atmosphere studies of TOI-270 d offered mantle-atmosphere chemical equilibration as a potential explanation for the measured molecular abundances (Benneke et al. 2024; Nixon et al. 2025), inferring that the high atmospheric metallicity can be explained without the need for initial accretion of abundant volatiles. In parallel, interior modeling work suggested that, instead, TOI-270 d might *not* have a molten surface (Breza et al. 2025). Within that study’s framework, theoretical lower limits on the mean molecular weight required for solidification range from $\mu \sim 2.7$ to 6 amu, depending on the 1-100 bar pressure range assumed for the radiative-convective boundary where the model transitions from an isothermal to an adiabatic temperature profile.

We find that when using instead realistic self-consistent atmosphere models coupled with interior models, the radiative-convective boundary systematically lies at pressures deeper than 100 bar, with some models not even reaching the convective zone at the bottom (1 kbar) of our atmosphere models. Careful consideration of the extent and temperature profile of the radiative layer is crucial, because it has a first-order impact on the determination of the planetary radius (Tang et al. 2024). None of the models that are consistent with TOI-270 d’s mass and radius in our framework have molten conditions at the mantle-atmosphere boundary, across the full $Z_{\text{env}} = 0.01$ to 1.0 range covered in this study. The mantle-atmosphere boundary instead occurs at pressures greater than 20 kbar, and temperatures of up to 2600 K, but remaining at lower temperatures than the high-pressure solidus of rock (Oganov & Ono 2004; Sakai et al. 2016). Silicate rock is in the bridgmanite phase at the boundary, except for $> 50\%$ envelope mass fractions where the post-perovskite phase is reached. Unless the $T_{\text{int}} = 25$ K assumed here is an underestimate to the extent that the radiative-convective boundary is reached at much lower pressures, or substantial mantle hydration pushes the solidus to lower temperatures (e.g., Katz et al. 2003), TOI-270 d should not have a magma ocean.

5. IMPACT FOR SUB-NEPTUNE STUDIES

Our modeling reveals that water-hydrogen demixing happens over a broad parameter space even at the warm 330–380 K temperatures explored in this work, which are high enough to avoid water condensation in the atmosphere, except for the lowest temperatures (only for

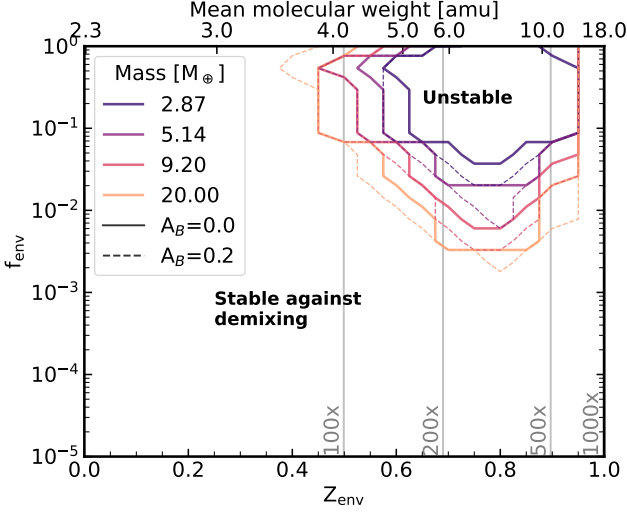


Figure 7. Contours delineating the region of parameter space where demixing occurs for different planet masses and Bond albedos, for a TOI-270 d-like irradiation level. The color encodes the planet mass, and the line style encodes Bond albedo (solid lines for $A_B = 0$, dashed for $A_B = 0.2$). Vertical gray lines indicate different atmosphere metallicities (labeled). None of the models shown cross the water condensation curve.

$A_B = 0.4$) and highest metallicities ($Z_{\text{env}} \simeq 1.0$). We explore the range of conditions where demixing should be expected on sub-Neptunes as well as the implications for sub-Neptune composition and thermal evolution modeling. We provide data products and open-source scripts to reproduce the contours of the demixing window as well as the mass-radius curves computed by ATHENAIA.

5.1. Demixing conditions

The ATHENAIA model grids are calculated for well-mixed envelopes (composition constant with pressure), and reveal that the calculated temperature profiles reach conditions of hydrogen-water immiscibility over a broad range of envelope mass fractions and envelope metal contents.

While demixing does not occur in the extreme water-only composition case ($Z_{\text{env}} = 1$) due to the steep increase in the pressure of the coexistence curve near $Z_{\text{env}} = 0.9$ (Fig. 4), the window in $f_{\text{env}} - Z_{\text{env}}$ space where demixing is predicted systematically extends to very metal-rich compositions, regardless of planet mass and Bond albedo (Figs. 7 and B1). The range of envelope mass fractions and metallicities where demixing occurs expands to lower values both with increasing Bond albedo and increasing planet mass, reaching metallicities of $< 100\times$ solar for a $20 M_{\oplus}$ planet.

Visualizing our constant-composition curves in mass-radius space reveals the importance of demixing at the population level for sub-Neptunes (Fig. 8). While not predicted for solar metallicity envelopes, as suggested by the deep pressures of the coexistence curves at low Z_{env} (Figs. 1 and 4), we find that even moderate $120\times$ solar metal enrichments can give rise to demixing for planets larger than $2.2 R_{\oplus}$ and with masses $> 4 M_{\oplus}$ in the $T_{\text{irr}} = 336 \text{ K}$ case ($A_B = 0.4$). While in these moderately metal-rich scenarios, the hotter $T_{\text{irr}} = 381 \text{ K}$ case ($A_B = 0.0$) is only unstable against demixing at the highest planet masses covered in the grid ($> 13 M_{\oplus}$), demixing conditions cover the entire mass-radius range of sub-Neptune conditions in the more metal-rich $250\times$ solar metallicity ($Z_{\text{env}} = 0.75$) case. This suggests that the $\gtrsim 100\times$ solar atmosphere metal enrichments typically inferred on sub-Neptunes (Hu et al. 2025; Benneke et al. 2024; Felix et al. 2025; Piaulet-Ghorayeb et al. 2024; Ahrer et al. 2025; Teske et al. 2025; Wallack et al. 2024) might instead reflect even more metal-enriched interiors.

5.2. Impact on composition and evolution

We find that rather than fully-mixed or layered-structure models, the envelopes of warm sub-Neptunes are to be described by a continuum of compositional gradient structures, with lower metallicities at low pressures and higher metallicities deeper down in the envelope, rather than a fully layered structure (as proposed for the ice giants; Amoros et al. 2024). Specifically, while envelopes with $\lesssim 100\times$ solar metallicity may be aptly described by fully-mixed models, our simple zeroth-order estimate of the amount of metal depletion to be expected in the upper atmosphere (as detailed in Sec. B.2) implies that the metallicities measured in the upper atmosphere via transmission spectroscopy are increasingly underestimating the bulk envelope metal mass content over the demixing window. Compositional stratification should have the strongest impact on the upper-atmosphere metallicities of colder and higher-mass planets with metal-rich envelopes, with predicted metal depletions of over 50% by mass predicted even at masses as low as $\sim 6 M_{\oplus}$. Meanwhile, planets with metallicities of $\sim 500\times$ solar and masses greater than $\sim 10 M_{\oplus}$ may be well represented by fully layered structures of near-solar-metallicity gas on top of a water-rich interior. This effect however also impacts low-mass sub-Neptunes: the upper-atmosphere metal mass content can be reduced by 20% even in the case of the lowest planetary mass ($2.86 M_{\oplus}$), zero-Bond-albedo (381K) explored in our grid.

Overall, using upper-atmosphere metallicities to represent the bulk envelope would result in an *underes-*

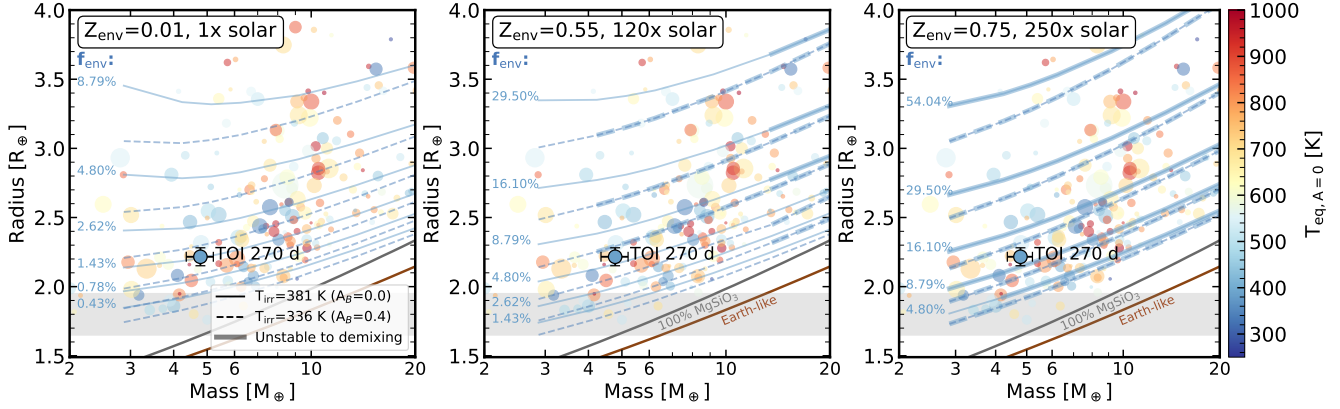


Figure 8. Mass-radius diagram of planets across the sub-Neptune size range (circles, colored by zero-Bond albedo equilibrium temperature) and their susceptibility to demixing for $Z_{\text{env}} = 0.01$ (left, $1\times$ solar metallicity), 0.55 (middle, $120\times$ solar metallicity), and 0.75 (right, $250\times$ solar metallicity). Circle sizes encode the favorability of planets to transmission spectroscopy via the transmission spectroscopy metric (Kempton et al. 2018). The position of TOI-270 d in mass-radius space is indicated by the opaque black-outlined circle, and constant-composition curves for an Earth-like and a 100% MgSiO_3 rocky composition (Zeng et al. 2016) are shown in grey and brown. The approximate position of the “radius valley” (Fulton et al. 2017) separating sub-Neptunes from the smaller rocky super-Earths is shown as the grey shaded area. For models of sub-Neptunes with gas envelopes, we show the ATHENAIA mass-radius relationships for various envelope mass fractions (labeled in each panel), for each envelope metallicity. The solid (dashed) curves are from the $A_B = 0.0$ ($A_B = 0.4$) model grid, colored in order to match the irradiation temperature they correspond to compared to the planet population. Thicker curves indicate conditions unstable to demixing. Over the 330–380 K temperature regime explored, demixing impacts sub-Neptunes across their entire range of masses and radii.

time of the envelope mass fraction, and therefore overestimated sub-Neptune core masses, over the range of conditions susceptible to demixing. In such a scenario, the upper atmosphere metallicity can no longer be used as a reasonable metric to break the mass-radius degeneracy between low-metallicity envelopes with lower mass fractions, and higher-metallicity envelopes with larger mass fractions (Fig. 8). Instead, interior-atmosphere modeling frameworks should be employed to model self-consistently the distribution of metals across the envelope and the corresponding temperature structure that result in structures fully stable against demixing. We expect a degeneracy in the measured atmosphere metallicities from transmission spectroscopy between intrinsically metal-poor envelopes (stable against demixing) and metal-enriched envelopes (unstable against demixing) which would have metal-depleted upper-atmospheres. This degeneracy may be less severe for the known sub-Neptunes with high upper-atmosphere metal enrichments, as those could only be achieved for intrinsically metal-rich envelopes.

While we only explored demixing over a limited range of insulations (irradiation temperatures from 336 to 381 K, representative of expected conditions on TOI-270 d), we observe a gradual “closing” of the demixing window for increasing insulations (Figs. 7 and B2). Extrapolating this behavior, we infer that to have stable fully-mixed conditions at the $Z_{\text{env}} = 0.8$ ($\sim 300\times$ solar

metallicity) enrichment where the propensity for demixing is maximized, irradiation temperatures of 400 K to 460 K (440 K to 500 K) are required for envelope mass fractions of $\leq 10\%$ ($\leq 50\%$).

Water-hydrogen demixing can have profound implications on the radius and thermal evolution of sub-Neptunes. The distribution of metals across the envelope would alter the cooling rate for a given internal entropy as well as impact the planet radius, and therefore the cross-section it offers to photoevaporative mass-loss. Further, mass-loss rates themselves would be higher for the same bulk envelope metallicities if compositional gradients exist, as the hydrogen-rich upper atmosphere may be more easily lost because of its lighter particle weight and less efficient metal cooling in the absence of abundant water (Piaulet-Ghorayeb et al. 2024; Kubyshkina, Egger & Piaulet-Ghorayeb, *subm.*). This work therefore motivates further exploration of the ramifications of sub-Neptune demixing in terms of the predictions of mass-loss and envelope thermal evolution models.

6. COMPARISON TO PREVIOUS STUDIES

We find that our modeling results are compatible with the current literature, and that the use of radiative-convective atmosphere models is essential to map the demixing window in $f_{\text{env}} - Z_{\text{env}}$ space.

First, our models reproduce the expected qualitative behavior of decreasing planet radius when increasing the envelope metallicity for a given planet mass and envelope mass fraction (Fig. 8). The range of envelope mass fractions predicted by ATHENAIA over the sub-Neptune size regime overall, and for TOI-270 d in particular, also matches expectations from models both at the H/He-rich (Lopez & Fortney 2014) and H₂O-rich (Aguichine et al. 2021) ends of the compositional range.

Our model setup for exploration of the susceptibility of planetary envelopes to demixing goes beyond previous work that adopted either fully adiabatic envelopes, or parameterized temperature profiles (Guillot 2010; Amoros et al. 2024; Howard et al. 2025), calculating composition-dependent radiative-convective temperature profiles as an upper boundary condition to the adiabatic interior models. This approach has several advantages. First, it allows for the self-consistent determination of the radiative-convective boundary (RCB) where the adiabatic profiles start, which we find to be deep and even > 1 kbar in some of our models, rather than the assumed, and often much lower, RCB pressures adopted ad-hoc when combining interior adiabats with parameterized functions in the upper atmosphere (Guillot 2010). Second, compared to using adiabatic profiles, our modeling approach accounts for the (often major; Tang et al. 2024) contribution of the radiative atmosphere to the planetary radius – which is the key observable for accurate composition estimation when linking planet observations to interior-atmosphere models.

We expanded upon previous single-planet, single-composition studies of the propensity of envelopes to demixing by instead systematically exploring its onset throughout the mass-radius diagram as a function of water content and over a small range of planetary irradiation conditions. We also proposed a new method to statistically assess the impact of demixing on the envelope composition of individual planets by leveraging mass, radius, irradiation, and atmospheric constraints. Taken together, this modeling exploration provides a first assessment of the impact of this process at the population level.

7. MODEL LIMITATIONS

The modeling work presented here has limitations related to the chosen prescription for demixing, envelope composition, and internal model assumptions.

First, while water condensation may, through the release of latent heat, heat up the planetary atmosphere – resulting in warmer interiors than we predict, and potentially impacting the diagnosis of hydrogen-water (im)miscibility, we find that our temperature profiles only

cross the water condensation curves in the coldest models with $A_B = 0.4$ and with high Z_{env} . Condensation is predicted for $Z_{\text{env}} > 0.95$ for masses up to $13 M_{\oplus}$ and > 0.9 over the 13 to $20 M_{\oplus}$ mass range (Fig. B2). These metallicities are so high that the conditions do not overlap with the demixing window for masses lower than $20 M_{\oplus}$, and should not impact our conclusions for most sub-Neptunes.

The main limitation of the atmosphere model is the set choice of T_{int} . We adopted $T_{\text{int}} = 25$ K, which is commonly adopted for sub-Neptunes (Madhusudhan et al. 2020; Kempton et al. 2023; Nixon et al. 2024), although the exact value will be dependent on each planet’s thermal evolution, and therefore on the atmosphere metallicity, envelope thickness, and any planetary eccentricity (see e.g. Lopez & Fortney 2014; Thorngren & Fortney 2018; Tang et al. 2024). For the purposes of this work, we choose this value because it is low enough to reveal the *potential* for envelope demixing under realistic conditions in sub-Neptune atmospheres, but high enough to remain realistic. While beyond the scope of this study, future work will evaluate the dependence of the demixing window on the compositionally-dependent thermal evolution, and whether the metal-rich sub-Neptune interiors that we proposed as demixing candidates ever get cool enough to match the assumptions made here.

We also note that while we adopt here Z_{atm} as a measure of water enrichment in a H₂-He-H₂O mixed atmosphere, atmosphere observations have shown that other species, including CH₄, are present in the atmosphere of TOI-270 d (Benneke et al. 2024; Holmberg & Madhusudhan 2024; Felix et al. 2025; Constantinou et al. 2025). Although the inferred water abundance is about 10 times larger than the methane content for TOI-270 d, the presence of carbon species could be a source of heating e.g. through graphite precipitation, depending on how the C/O ratio varies throughout the atmosphere (Peng & Valencia 2024), or otherwise impact the atmospheric temperature-pressure profile due to their large infrared cross-sections. To our knowledge, no study has yet studied the miscibility of water and hydrogen in the presence of carbon species.

As mentioned in a few instances in the discussion, some models do not reach the RCB even at 1 kbar, which is a known issue in linking atmosphere and interior models (Kempton et al. 2023; Nixon et al. 2024; Aguichine et al. 2024). However, we do not expect that this would impact our conclusion that demixing is possible on sub-Neptunes: instead, a deeper RCB would lead to an even colder interior in our models, which would be more prone to demixing.

For the prescription adopted to calculate the coexistence curves, we used the results from [Gupta et al. \(2024\)](#). Although other studies have explored hydrogen-water miscibility using either a parameterized force field instead of DFT, or DFT calculations but determining the solvus using free energies rather than phase coexistence, the reference we adopt provides a better match to experimental data and spans a wider range of temperatures down to 750 K ([Bergermann et al. 2021, 2024](#); [Soubiran & Militzer 2015](#)). Even if demixing is predicted by our models, we note that convective overshoot may partially counteract it and transport metal-rich material to lower pressures. Future models should explore whether the depth of the metal-rich region and the mixing length could sustain envelope compositional homogeneity even when a H_2 - H_2O mixed phase is thermodynamically disfavored.

In terms of the interior model, we only explore Earth-like ratios of iron and silicates in the interior, but the range of compositions consistent with demixing might extend further throughout the parameter space if studied over a wider range of f'_{core} values. On the other hand, the interior we model does not account for silicate-hydrogen miscibility which could lower the density of the mantle ([Rogers et al. 2025](#); [Young et al. 2025](#)) and reduce the range of envelope compositions that reach the deep pressures required for demixing above the MEB. Besides, one of the largest sources of uncertainty in interior models lies in the assumed material properties and the choice of EOS, and our conclusions may be impacted by future improvements to e.g. the hydrogen or water EOS, if they substantially impact the densities and adiabatic gradients over the T-P range we consider.

8. SUMMARY AND CONCLUSIONS

In this work, we performed an exploration of the extent to which water-hydrogen demixing can impact the compositions of sub-Neptune envelopes, for planets too warm for water condensation. We used the ATHENAIA framework introduced in this work to explore compositions ranging from solar-metallicity, H_2/He -dominated all the way to pure- H_2O using coupled atmosphere-interior models, and evaluated the compatibility of the envelope thermodynamic conditions with fully-mixed compositions for irradiation levels comparable to TOI-270 d.

We find that even if more metal-rich atmospheres are hotter, their shallower adiabatic gradients in the deep envelope, combined with the shift of the hydrogen-water coexistence curve to higher temperatures when metallicities approach $200\times$ solar, open a window for demixing

even if water is in the supercritical state on warm, metal-rich sub-Neptunes.

We use our coupled interior-atmosphere models to infer the joint constraints on the envelope mass fractions and metallicities compatible with TOI-270 d’s bulk properties, and find substantial overlap between the inferred properties of TOI-270 d’s envelope and the demixing window, which also coincide with the measured atmosphere metallicity from JWST observations ([Benneke et al. 2024](#)). Therefore, unless the true upper atmosphere metallicity is close to the lower end allowed by atmosphere constraints (near $100\times$ solar), TOI-270 d’s envelope structure could exhibit a compositional gradient rather than having a fully miscible envelope as previously proposed. This would imply an even larger bulk envelope metallicity than measured in the upper atmosphere.

Overall, demixing affects less irradiated planets as well as more massive planets over a wider range of envelope mass fractions and metallicities, although even $\lesssim 3M_{\oplus}$ planets can experience substantial demixing for enhanced bulk envelope metallicities. We find that warm sub-Neptunes between irradiation temperatures of approximately 330 K and 500 K are impacted throughout the mass-radius diagram, and increasingly so for high $\gtrsim 200\times$ solar metallicities.

We provide a new set of open-source constant-composition mass-radius curves calculated with ATHENAIA for the three irradiation levels explored in this study, the first one to span the full range of compositions from H/He -dominated to H_2O -dominated. We also share the $Z_{\text{stable}}/Z_{\text{env}}$ metric (Fig. B2) that encodes the envelope’s stability to demixing throughout our model grid, as well as a script that can be used to draw the demixing contours on the $f_{\text{env}} - Z_{\text{env}}$ plane.

Although we identified demixing as a process that can impact even warm sub-Neptunes, thermal evolution calculations are necessary to track how the mass- and metallicity-dependence of the cooling rate in exoplanetary atmosphere changes this picture after Gyr of evolution. We also encourage further exploration of the range of stellar irradiation environments where demixing is to be expected, as we find it to affect even our highest-temperature simulations at $T_{\text{irr}} = 380$ K and estimate its impact extends up to $T_{\text{irr}} = 500$ K. Identifying sub-Neptunes with truly fully-miscible envelopes, or quantifying the extent of the mismatch between upper atmosphere and bulk metallicities, will be crucial to interpret observations of sub-Neptune atmospheres in terms of their formation building blocks.

9. DATA AVAILABILITY

The mass-radius curves and demixing contours calculated in this work are provided at the Zenodo link associated with this study.

Acknowledgments—C. P.-G. thanks Hamish Innes, Raymond Pierrehumbert, Thaddeus Komacek, and Joseph Schools for helpful conversations on the topic of hydrogen-water miscibility and mantle melting. This work is based on observations with the

NASA/ESA/CSA James Webb Space Telescope, obtained at the Space Telescope Science Institute (STScI) operated by AURA, Inc. C.P.-G. acknowledges support from the E. Margaret Burbidge Prize Postdoctoral Fellowship from the Brinson Foundation.

Software: PHOENIX (Husser et al. 2013), `astropy`⁶ (Astropy Collaboration et al. 2013), `numpy`⁷ (Harris et al. 2020), `matplotlib`⁸ (Hunter 2007), `scipy`⁹ (Virtanen et al. 2020) `astropy`¹⁰ (Astropy Collaboration et al. 2013) `pytorch`¹¹ (Paszke et al. 2019)

APPENDIX

A. ATMOSPHERE TEMPERATURE PROFILE DETERMINATION

To compute the atmospheric temperature profile in radiative-convective equilibrium with SCARLET, we employ an iterative solver following the Toon et al. (1989) linearization approach, adapted for non-gray opacities and flexible convection handling. The method alternates between radiative flux optimization and convective adjustment, and we implemented `pytorch`-based GPU acceleration (Paszke et al. 2019) to employ vectorization for the most computationally-expensive steps.

Radiative Equilibrium Iteration—Starting from an initial-guess temperature-pressure (T-P) profile, and repeating after each new T-P profile iteration, we perform the hydrostatic equilibrium calculation and compute the opacity terms. We calculate the upward and downward thermal fluxes by solving two-stream, multi-scattering radiative transfer by adapting the routine implemented in PICASO (Batalha et al. 2019) for the Toon et al. (1989) method.

The resulting radiative fluxes are used to calculate local heating (i.e., flux divergence). The linearization step is performed by constructing the Jacobian of net fluxes with respect to temperature, exploiting automatic differentiation with `pytorch` for efficient computation of the Jacobian matrix. The temperature correction is then obtained by solving the resulting linear system, with adaptive temperature step size reduction for stability. Radiative equilibrium is considered achieved when per-layer temperature changes and the number of unconverged layers meet thresholds of proposed temperature changes of less than 10^{-3} K.

Convective Adjustment—Superadiabatic layers are identified after the radiative-equilibrium T-P profile update. We compare the temperature gradient to the adiabatic gradient, ∇_{ad} , computed at the same composition by the interior modeling code and interpolated at the atmosphere model layer’s temperature and pressure (linear interpolation in the temperature dimension, and log interpolation in the pressure dimension).

The temperature profile is iteratively modified with temperatures in the superadiabatic layers are recursively adjusted to the environmental lapse rate, since superadiabatic temperature gradients are not expected in the absence of compositional gradients. The process is repeated until no superadiabatic layer remains, and we iterate over the radiative transfer and hydrostatic equilibrium steps, adjusting the temperature in the non-convective layers until both radiative and convective processes self-consistently reach equilibrium.

B. ADDITIONAL MODEL GRID PRODUCTS

B.1. Envelope temperature profiles

We illustrate in Fig. B1 the range of temperature-pressure conditions spanned by our models across the grid for all masses, metallicities, albedos, and envelope mass fractions.

⁶ <https://www.astropy.org/>

⁷ <https://github.com/numpy/numpy>

⁸ <https://github.com/matplotlib/matplotlib>

⁹ <https://github.com/scipy/scipy>

¹⁰ <https://github.com/astropy/astropy>

¹¹ <https://github.com/pytorch/pytorch/>

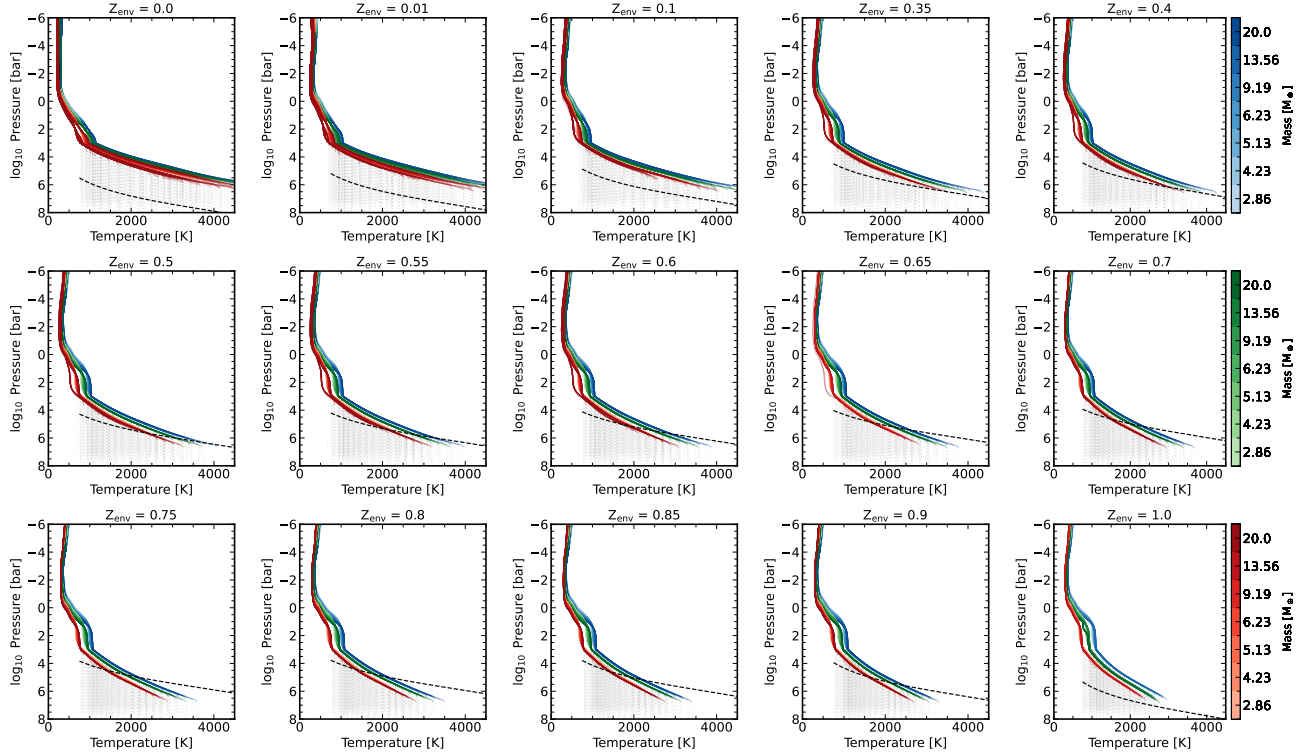


Figure B1. Temperature-pressure profile for the envelope (colors) and interior (dotted, gray) across all conditions in the grid, compared to the coexistence curves (black, dashed) for different envelope metallicities (labeled for each panel). The color shading encode the planet mass for the three albedos (shades of blue for $A_B = 0.0$, green for 0.2, red for 0.4). The vertical and horizontal span in temperature-pressure space is kept constant throughout all panels to illustrate the compositional dependence of the demixing window.

B.2. Estimate of stable upper-atmosphere metallicities

We calculate a simple estimate of the extent of demixing in the upper atmosphere by computing the value of Z where the temperature at the first unstable point from the top of the atmosphere (pressure level where the coexistence curve is crossed) would instead remain stable against demixing. We visualize this “stable Z ” value (Z_{stable}) for the upper envelope over the parameter space where our model predicts demixing (Fig. B2).

Although this informs the magnitude of upper-atmosphere demixing, in reality, the temperature profile and ambient metallicity should be iterated over until the metals have been spread across the envelope in a way that stability against demixing is achieved in each atmosphere layer (Amoros et al. 2024), and this exploration should only be considered as illustrative rather than a quantitative assessment, which is beyond the scope of the present study.

REFERENCES

- Aguichine, A., Batalha, N., Fortney, J. J., et al. 2024, Evolution of steam worlds: energetic aspects, arXiv, doi: [10.48550/arXiv.2412.17945](https://doi.org/10.48550/arXiv.2412.17945)
- Aguichine, A., Mousis, O., Deleuil, M., & Marcq, E. 2021, arXiv e-prints, 2105, arXiv:2105.01102. <http://adsabs.harvard.edu/abs/2021arXiv210501102A>
- Ahrer, E.-M., Radica, M., Piaulet-Ghorayeb, C., et al. 2025, doi: [10.3847/2041-8213/add010](https://doi.org/10.3847/2041-8213/add010)
- Alibert, Y., & Benz, W. 2017, *Astronomy & Astrophysics*, 598, L5, doi: [10.1051/0004-6361/201629671](https://doi.org/10.1051/0004-6361/201629671)
- Amoros, M. C., Nettelmann, N., Tosi, N., Baumeister, P., & Rauer, H. 2024, $\text{H}_2\text{-H}_2\text{SO}$ demixing in Uranus and Neptune: Adiabatic structure models, arXiv. <http://arxiv.org/abs/2410.21099>
- Arevalo, R. T. 2025, Different Inhomogeneous Evolutionary Histories for Uranus and Neptune, arXiv, doi: [10.48550/arXiv.2506.13857](https://doi.org/10.48550/arXiv.2506.13857)
- Astropy Collaboration, Robitaille, T. P., Tollerud, E. J., et al. 2013, *Astronomy and Astrophysics*, 558, A33, doi: [10.1051/0004-6361/201322068](https://doi.org/10.1051/0004-6361/201322068)

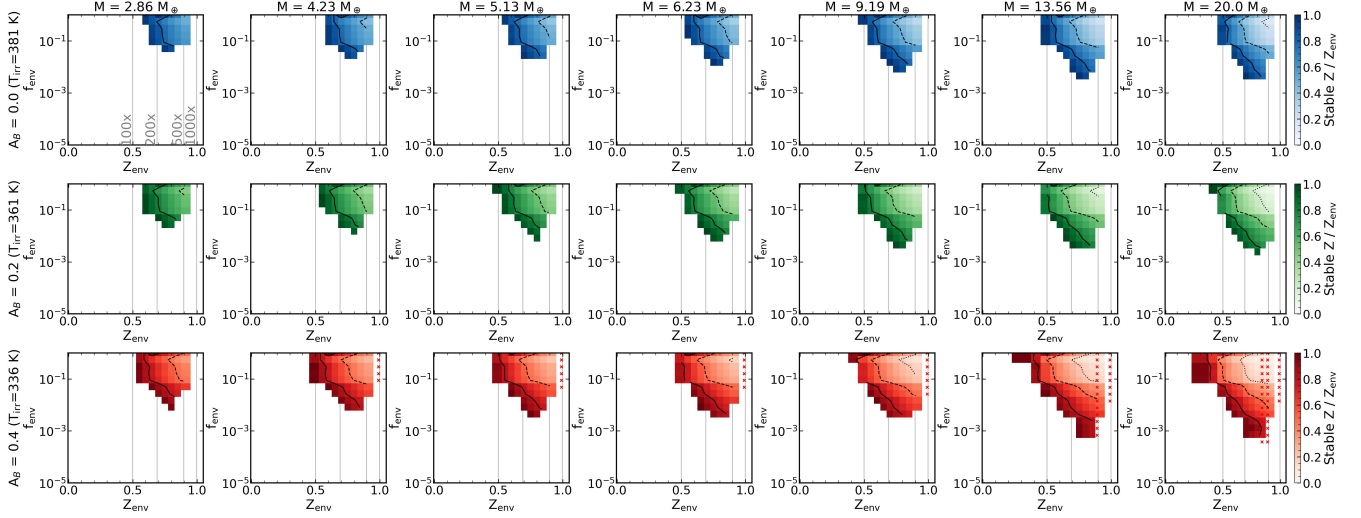


Figure B2. Metal depletion in the upper envelope relative to the bulk envelope metallicity, throughout the demixing window (where the stable Z is lower than the bulk Z), as a function of irradiation or Bond albedo (different rows) and planet mass (different columns). Vertical grey lines are added to guide interpretation in terms of the envelope metallicity relative to solar (labeled in the first panel). Not only does the demixing window expand in both dimensions of envelope mass fraction and envelope metallicity as the insolation decreases and planetary mass increases, but the extent of expected metal depletion in the upper envelope simultaneously becomes more severe. Black contours indicate upper envelope metal depletion (in units of Z) of 20% (solid), 50% (dashed), and 80% (dotted). Profiles where water condensation is predicted in the upper atmosphere are indicated with crosses. The area where no demixing is predicted in our models is left in white.

Batalha, N. E., Marley, M. S., Lewis, N. K., & Fortney, J. J. 2019, *The Astrophysical Journal*, 878, 70, doi: [10.3847/1538-4357/ab1b51](https://doi.org/10.3847/1538-4357/ab1b51)

Batalha, N. M., Rowe, J. F., Bryson, S. T., et al. 2013, *The Astrophysical Journal Supplement Series*, 204, 24, doi: [10.1088/0067-0049/204/2/24](https://doi.org/10.1088/0067-0049/204/2/24)

Benneke, B. 2013, American Astronomical Society Meeting Abstracts #221, 221, 224.04. <https://ui.adsabs.harvard.edu/abs/2013AAS...22122404B/abstract>

Benneke, B., & Seager, S. 2012, *The Astrophysical Journal*, 753, 100, doi: [10.1088/0004-637X/753/2/100](https://doi.org/10.1088/0004-637X/753/2/100)

Benneke, B., Knutson, H. A., Lothringer, J., et al. 2019, *Nature Astronomy*, 3, 813, doi: [10.1038/s41550-019-0800-5](https://doi.org/10.1038/s41550-019-0800-5)

Benneke, B., Roy, P.-A., Coulombe, L.-P., et al. 2024, JWST Reveals CH₄, CO₂, and H₂O in a Metal-rich Miscible Atmosphere on a Two-Earth-Radius Exoplanet, arXiv. [http://arxiv.org/abs/2403.03325](https://arxiv.org/abs/2403.03325)

Bergermann, A., French, M., & Redmer, R. 2021, *Physical Chemistry Chemical Physics*, 23, 12637, doi: [10.1039/D1CP00515D](https://doi.org/10.1039/D1CP00515D)

—. 2024, *Physical Review B*, 109, 174107, doi: [10.1103/PhysRevB.109.174107](https://doi.org/10.1103/PhysRevB.109.174107)

Breza, B., Nixon, M. C., & Kempton, E. M.-R. 2025, Not All Sub-Neptune Exoplanets Have Magma Oceans, arXiv, doi: [10.48550/arXiv.2509.20429](https://doi.org/10.48550/arXiv.2509.20429)

Burn, R., Mordasini, C., Mishra, L., et al. 2024, A radius valley between migrated steam worlds and evaporated rocky cores, arXiv. [http://arxiv.org/abs/2401.04380](https://arxiv.org/abs/2401.04380)

Chabrier, G., Mazevet, S., & Soubiran, F. 2019, *The Astrophysical Journal*, 872, 51, doi: [10.3847/1538-4357/aaf99f](https://doi.org/10.3847/1538-4357/aaf99f)

Constantinou, S., Madhusudhan, N., & Holmberg, M. 2025, The atmospheric composition of TOI-270 d, arXiv, doi: [10.48550/arXiv.2511.13830](https://doi.org/10.48550/arXiv.2511.13830)

Eylen, V. V., Astudillo-Defru, N., Bonfils, X., et al. 2021, *Monthly Notices of the Royal Astronomical Society*, stab2143, doi: [10.1093/mnras/stab2143](https://doi.org/10.1093/mnras/stab2143)

Felix, L., Kitzmann, D., Demory, B.-O., & Mordasini, C. 2025, doi: [10.48550/arXiv.2504.13039](https://doi.org/10.48550/arXiv.2504.13039)

Fulton, B. J., & Petigura, E. A. 2018, *The Astronomical Journal*, 156, 264, doi: [10.3847/1538-3881/aae828](https://doi.org/10.3847/1538-3881/aae828)

Fulton, B. J., Petigura, E. A., Howard, A. W., et al. 2017, *The Astronomical Journal*, 154, 109, doi: [10.3847/1538-3881/aa80eb](https://doi.org/10.3847/1538-3881/aa80eb)

Guillot, T. 2010, *Astronomy and Astrophysics*, 520, A27, doi: [10.1051/0004-6361/200913396](https://doi.org/10.1051/0004-6361/200913396)

Gupta, A., & Schlichting, H. E. 2020, arXiv:1907.03732 [astro-ph]. [http://arxiv.org/abs/1907.03732](https://arxiv.org/abs/1907.03732)

Gupta, A., Stixrude, L., & Schlichting, H. E. 2024, The miscibility of hydrogen and water in planetary atmospheres and interiors, doi: [10.48550/arXiv.2407.04685](https://doi.org/10.48550/arXiv.2407.04685)

- Harris, C. R., Millman, K. J., van der Walt, S. J., et al. 2020, *Nature*, 585, 357, doi: [10.1038/s41586-020-2649-2](https://doi.org/10.1038/s41586-020-2649-2)
- Holmberg, M., & Madhusudhan, N. 2024, Possible Hycean conditions in the sub-Neptune TOI-270 d, doi: [10.1051/0004-6361/202348238](https://doi.org/10.1051/0004-6361/202348238)
- Howard, A. W., Marcy, G. W., Bryson, S. T., et al. 2012, *ApJS*, 201, 15, doi: [10.1088/0067-0049/201/2/15](https://doi.org/10.1088/0067-0049/201/2/15)
- Howard, S., Helled, R., Bergermann, A., & Redmer, R. 2025, The Possibility of Hydrogen-Water Demixing in Uranus, Neptune, K2-18b and TOI-270d, arXiv, doi: [10.48550/arXiv.2507.06288](https://doi.org/10.48550/arXiv.2507.06288)
- Hu, R., Bello-Arufe, A., Tokadjian, A., et al. 2025, A water-rich interior in the temperate sub-Neptune K2-18 b revealed by JWST, arXiv, doi: [10.48550/arXiv.2507.12622](https://doi.org/10.48550/arXiv.2507.12622)
- Hunter, J. D. 2007, *Computing in Science and Engineering*, 9, 90, doi: [10.1109/MCSE.2007.55](https://doi.org/10.1109/MCSE.2007.55)
- Husser, T.-O., Wende-von Berg, S., Dreizler, S., et al. 2013, *Astronomy & Astrophysics*, Volume 553, id.A6, <NUMPAGES>9</NUMPAGES> pp., 553, A6, doi: [10.1051/0004-6361/201219058](https://doi.org/10.1051/0004-6361/201219058)
- Innes, H., Tsai, S.-M., & Pierrehumbert, R. T. 2023, *The Astrophysical Journal*, 953, 168, doi: [10.3847/1538-4357/ace346](https://doi.org/10.3847/1538-4357/ace346)
- Katz, R. F., Spiegelman, M., & Langmuir, C. H. 2003, *Geochemistry, Geophysics, Geosystems*, 4, doi: [10.1029/2002GC000433](https://doi.org/10.1029/2002GC000433)
- Kempton, E. M. R., Lessard, M., Malik, M., et al. 2023, *The Astrophysical Journal*, 953, 57, doi: [10.3847/1538-4357/ace10d](https://doi.org/10.3847/1538-4357/ace10d)
- Kempton, E. M.-R., Bean, J. L., Louie, D. R., et al. 2018, *Publications of the Astronomical Society of the Pacific*, 130, 114401, doi: [10.1088/1538-3873/aadf6f](https://doi.org/10.1088/1538-3873/aadf6f)
- Kite, E. S., & Schaefer, L. 2021, *The Astrophysical Journal*, 909, L22, doi: [10.3847/2041-8213/abe7dc](https://doi.org/10.3847/2041-8213/abe7dc)
- Kuchner, M. J. 2003, *The Astrophysical Journal Letters*, 596, L105, doi: [10.1086/378397](https://doi.org/10.1086/378397)
- Lichtenberg, T. 2021, *The Astrophysical Journal*, 914, L4, doi: [10.3847/2041-8213/ac0146](https://doi.org/10.3847/2041-8213/ac0146)
- Lichtenberg, T., Drazkowska, J., Schonbachler, M., Golabek, G. J., & Hands, T. O. 2021, *Science*, 371, 365, doi: [10.1126/science.abb3091](https://doi.org/10.1126/science.abb3091)
- Lodders, K. 2010, arXiv:1010.2746 [astro-ph], 379, doi: [10.1007/978-3-642-10352-0_8](https://doi.org/10.1007/978-3-642-10352-0_8)
- Lopez, E. D., & Fortney, J. J. 2014, *The Astrophysical Journal*, 792, 1, doi: [10.1088/0004-637X/792/1/1](https://doi.org/10.1088/0004-637X/792/1/1)
- Luque, R., & Pallé, E. 2022, *Science*, 377, 1211, doi: [10.1126/science.abl7164](https://doi.org/10.1126/science.abl7164)
- Madhusudhan, N., Nixon, M. C., Welbanks, L., Piette, A. A., & Booth, R. A. 2020, *The Astrophysical Journal Letters*, 891, L7, doi: [10.3847/2041-8213/ab7229](https://doi.org/10.3847/2041-8213/ab7229)
- Madhusudhan, N., Piette, A. A., & Constantinou, S. 2021, *The Astrophysical Journal*, 918, 1, doi: [10.3847/1538-4357/abfd9c](https://doi.org/10.3847/1538-4357/abfd9c)
- Mazevet, S., Licari, A., Chabrier, G., & Potekhin, A. Y. 2019, *Astronomy and Astrophysics*, 621, A128, doi: [10.1051/0004-6361/201833963](https://doi.org/10.1051/0004-6361/201833963)
- Miller-Ricci, E., Seager, S., & Sasselov, D. 2009, *The Astrophysical Journal*, 690, 1056, doi: [10.1088/0004-637X/690/2/1056](https://doi.org/10.1088/0004-637X/690/2/1056)
- More, R. M., Warren, K. H., Young, D. A., & Zimmerman, G. B. 1988, *Physics of Fluids*, 31, 3059, doi: [10.1063/1.866963](https://doi.org/10.1063/1.866963)
- Neil, A. R., Liston, J., & Rogers, L. A. 2022, arXiv:2205.00006 [astro-ph], <http://arxiv.org/abs/2205.00006>
- Nettelmann, N., Fortney, J. J., Kramm, U., & Redmer, R. 2011, *The Astrophysical Journal*, 733, 2, doi: [10.1088/0004-637X/733/1/2](https://doi.org/10.1088/0004-637X/733/1/2)
- Nettelmann, N., Holst, B., Kietzmann, A., et al. 2008, *The Astrophysical Journal*, 683, 1217, doi: [10.1086/589806](https://doi.org/10.1086/589806)
- Nixon, M. C., Piette, A. A., Kempton, E. M.-R., et al. 2024, New insights into the internal structure of GJ 1214 b informed by JWST, arXiv, <http://arxiv.org/abs/2407.12079>
- Nixon, M. C., Somers, R. S., Savel, A. B., et al. 2025, Magma ocean interactions can explain JWST observations of the sub-Neptune TOI-270 d, arXiv, doi: [10.48550/arXiv.2510.07367](https://doi.org/10.48550/arXiv.2510.07367)
- Oganov, A. R., & Ono, S. 2004, *Nature*, 430, 445, doi: [10.1038/nature02701](https://doi.org/10.1038/nature02701)
- Owen, J. E., & Wu, Y. 2017, *The Astrophysical Journal*, 847, 29, doi: [10.3847/1538-4357/aa890a](https://doi.org/10.3847/1538-4357/aa890a)
- Paszke, A., Gross, S., Massa, F., et al. 2019, *PyTorch: An Imperative Style, High-Performance Deep Learning Library*, arXiv, doi: [10.48550/arXiv.1912.01703](https://doi.org/10.48550/arXiv.1912.01703)
- Peng, B., & Valencia, D. 2024, <http://arxiv.org/abs/2405.08998>
- Piaulet, C., Benneke, B., Almenara, J. M., et al. 2023, *Nature Astronomy*, 7, 206, doi: [10.1038/s41550-022-01835-4](https://doi.org/10.1038/s41550-022-01835-4)
- Piaulet-Ghorayeb, C., Benneke, B., Radica, M., et al. 2024, *The Astrophysical Journal Letters*, 974, L10, doi: [10.3847/2041-8213/ad6f00](https://doi.org/10.3847/2041-8213/ad6f00)
- Pierrehumbert, R. T. 2022, The runaway greenhouse on subNeptune waterworlds, arXiv, doi: [10.48550/arXiv.2212.02644](https://doi.org/10.48550/arXiv.2212.02644)

- Rigby, F. E., & Madhusudhan, N. 2025, The Surface and Interior Conditions of Temperate Sub-Neptune TOI-270 d, arXiv, doi: [10.48550/arXiv.2511.16722](https://doi.org/10.48550/arXiv.2511.16722)
- Rogers, J. G., Gupta, A., Owen, J. E., & Schlichting, H. E. 2021, Monthly Notices of the Royal Astronomical Society, 508, 5886, doi: [10.1093/mnras/stab2897](https://doi.org/10.1093/mnras/stab2897)
- Rogers, J. G., Schlichting, H. E., & Owen, J. E. 2023, Conclusive evidence for a population of water-worlds around M-dwarfs remains elusive, arXiv. <http://arxiv.org/abs/2301.04321>
- Rogers, J. G., Young, E. D., & Schlichting, H. E. 2025, Redefining interiors and envelopes: hydrogen-silicate miscibility and its consequences for the structure and evolution of sub-Neptunes, arXiv, doi: [10.48550/arXiv.2509.13320](https://doi.org/10.48550/arXiv.2509.13320)
- Rogers, L. A., & Seager, S. 2010, The Astrophysical Journal, 712, 974, doi: [10.1088/0004-637X/712/2/974](https://doi.org/10.1088/0004-637X/712/2/974)
- Roy, P.-A., Benneke, B., Piaulet, C., et al. 2022, The Astrophysical Journal, 941, 89, doi: [10.3847/1538-4357/ac9f18](https://doi.org/10.3847/1538-4357/ac9f18)
- Sakai, T., Dekura, H., & Hirao, N. 2016, Scientific Reports, 6, 22652, doi: [10.1038/srep22652](https://doi.org/10.1038/srep22652)
- Schlichting, H. E., & Young, E. D. 2021, Chemical equilibrium between Cores, Mantles, and Atmospheres of Super-Earths and Sub-Neptunes, and Implications for their Compositions, Interiors and Evolution, Tech. rep. <https://ui.adsabs.harvard.edu/abs/2021arXiv210710405S>
- . 2022, The Planetary Science Journal, 3, 127, doi: [10.3847/PSJ/ac68e6](https://doi.org/10.3847/PSJ/ac68e6)
- Seward, T. M., & Franck, E. U. 1981, Berichte der Bunsengesellschaft für physikalische Chemie, 85, 2, doi: [10.1002/bbpc.19810850103](https://doi.org/10.1002/bbpc.19810850103)
- Soubiran, F., & Militzer, B. 2015, The Astrophysical Journal, 806, 228, doi: [10.1088/0004-637X/806/2/228](https://doi.org/10.1088/0004-637X/806/2/228)
- Tang, Y., Fortney, J. J., Nimmo, F., et al. 2024, Reassessing Sub-Neptune Structure, Radii, and Thermal Evolution, arXiv. <http://arxiv.org/abs/2410.21584>
- Teske, J., Batalha, N. E., Wallack, N. L., et al. 2025, JWST COMPASS: NIRSpec/G395H Transmission Observations of TOI-776 c, a 2 Rearth M Dwarf Planet, doi: [10.48550/arXiv.2502.20501](https://doi.org/10.48550/arXiv.2502.20501)
- Thompson, S. L. 1990, ANEOS—Analytic Equations of State for Shock Physics Codes
- Thorngren, D., & Fortney, J. J. 2019, The Astrophysical Journal, 874, L31, doi: [10.3847/2041-8213/ab1137](https://doi.org/10.3847/2041-8213/ab1137)
- Thorngren, D. P. 2019, Ph.D. thesis. <https://ui.adsabs.harvard.edu/abs/2019PhDT.....51T>
- Thorngren, D. P., & Fortney, J. J. 2018, The Astronomical Journal, 155, 214, doi: [10.3847/1538-3881/aaba13](https://doi.org/10.3847/1538-3881/aaba13)
- Thorngren, D. P., Fortney, J. J., Murray-Clay, R. A., & Lopez, E. D. 2016, The Astrophysical Journal, 831, 64, doi: [10.3847/0004-637X/831/1/64](https://doi.org/10.3847/0004-637X/831/1/64)
- Toon, O. B., McKay, C. P., Ackerman, T. P., & Santhanam, K. 1989, Journal of Geophysical Research, 94, 16287, doi: [10.1029/JD094iD13p16287](https://doi.org/10.1029/JD094iD13p16287)
- Turbet, M., Bolmont, E., Ehrenreich, D., et al. 2020, Astronomy & Astrophysics, Volume 638, id.A41, <NUMPAGES>10</NUMPAGES> pp., 638, A41, doi: [10.1051/0004-6361/201937151](https://doi.org/10.1051/0004-6361/201937151)
- Virtanen, P., Gommers, R., Oliphant, T. E., et al. 2020, Nature Methods, 17, 261, doi: [10.1038/s41592-019-0686-2](https://doi.org/10.1038/s41592-019-0686-2)
- Wallack, N. L., Batalha, N. E., Alderson, L., et al. 2024, JWST COMPASS: A NIRSpec/G395H Transmission Spectrum of the Sub-Neptune TOI-836c, arXiv. <http://arxiv.org/abs/2404.01264>
- Werlen, A., Dorn, C., Burn, R., et al. 2025a, The Astrophysical Journal, 991, L16, doi: [10.3847/2041-8213/adff73](https://doi.org/10.3847/2041-8213/adff73)
- Werlen, A., Dorn, C., Schlichting, H. E., Grimm, S. L., & Young, E. D. 2025b, Atmospheric C/O Ratios of Sub-Neptunes with Magma Oceans: Homemade rather than Inherited, arXiv, doi: [10.48550/arXiv.2504.20450](https://doi.org/10.48550/arXiv.2504.20450)
- Young, E. D., Werlen, A., Marcum, S. P., & Dullemond, C. P. 2025, doi: [10.48550/arXiv.2507.00947](https://doi.org/10.48550/arXiv.2507.00947)
- Zeng, L., Sasselov, D. D., & Jacobsen, S. B. 2016, The Astrophysical Journal, 819, 127, doi: [10.3847/0004-637X/819/2/127](https://doi.org/10.3847/0004-637X/819/2/127)
- Zeng, L., Jacobsen, S. B., Sasselov, D. D., et al. 2019, Proceedings of the National Academy of Science, 116, 9723, doi: [10.1073/pnas.1812905116](https://doi.org/10.1073/pnas.1812905116)